nature communications

Article

https://doi.org/10.1038/s41467-025-65342-6

Bichromatic moiré superlattices for tunable quadrupolar trions and correlated states

Received: 3 September 2025

Accepted: 10 October 2025

Published online: 24 November 2025

Check for updates

Mingfeng Chen[1,8], Runtong Li[1,8], Haonan Wang[1,8], Yuliang Yang[1], Yiyang Lai[1], Chaowei Hu[2], Takashi Taniguchi[3], Kenji Watanabe[4], Jiaqiang Yan[5], Jiun-Haw Chu[2], Erik Henriksen[1,6,7], Chuanwei Zhang[1,6,7], Li Yang[1,6,7] & Xi Wang[1,6,7]

Moiré superlattices in transition metal dichalcogenide heterostructures provide a platform to engineer many-body interactions. Here, we realize a bichromatic moiré superlattice in an asymmetric $WSe_2/WS_2/WSe_2$ heterotrilayer by combining R- and H-stacked bilayers with mismatched moiré wavelengths. This structure hosts fermionic quadrupolar moiré trions—interlayer excitons bound to an opposite-layer hole—with vanishing dipole moments. These trions arise from hybridized moiré potentials enabling multiple excitonic orbitals with tunable interlayer coupling, allowing control of excitonic and electronic ground states. We show that an out-of-plane electric field could effectively reshape moiré excitons and interlayer-intralayer electron correlations, driving a transition from interlayer to intralayer Mott states with enhanced Coulomb repulsion. The asymmetric stacking further enriches excitonic selection rules, broadening opportunities for spin-photon engineering. Our results demonstrate bichromatic moiré superlattices as a reconfigurable platform for emergent quantum states, where quadrupolar moiré trion emission may enable coherent and entangled quantum light manipulation.

When two or more 2D layers in a heterostructure have slightly different lattice constants or are oriented in a way that their periodicities do not perfectly align, they create a moiré pattern, i.e., moiré superlattice. It dictates various physical properties such as the electronic band structures and excitonic states et al.[1–7]. Moiré superlattices demonstrate significant potentials for studying many-body interactions, including excitonic complexes (e.g., trions, biexcitons)[8–10], for quantum simulations such as Hubbard model physics[11–15]. The creation of moiré superlattices in transition metal dichalcogenide (TMD) heterostructures has revealed or predicted a diverse range of phases in these systems, including generalized Wigner crystals[16–23], Mott insulators[12,18,24], bosonic (excitonic) insulators[20,25–29], charge transfer insulators[30], as well as fractional[31–34] and integer[35] quantum anomalous states.

While enhancing the versatility of superlattice landscapes opens up a spectrum of possibilities, the inherent rigidity in these heterostructural moiré superlattices presents a significant challenge for post-fabrication tuning. One promising method is to harness the interference of distinct moiré wavelengths to craft intricate, tunable bichromatic patterns[36]. While theoretical insights have demonstrated the potential of creating adjustable multi-chromatic superlattices within TMD heterotrilayers to leverage moiré potentials from

[1]Department of Physics, Washington University, St. Louis, MO, USA. [2]Department of Physics, University of Washington, Seattle, WA, USA. [3]Research Center for Materials Nanoarchitectonics, National Institute for Materials Science, Tsukuba, Japan. [4]Research Center for Electronic and Optical Materials, National Institute for Materials Science, Tsukuba, Japan. [5]Materials Science and Technology Division, Oak Ridge National Laboratory, Oak Ridge, TN, USA. [6]Center for Quantum Leaps, Washington University, St. Louis, MO, USA. [7]Institute of Materials Science and Engineering, Washington University, St. Louis, MO, USA. [8]These authors contributed equally: Mingfeng Chen, Runtong Li, Haonan Wang. e-mail: wxi@wustl.edu

independently controlled heterointerfaces across layered structures, the experimental realization remains absent. Key open questions include how different moiré potentials interact and coevolve, how charge redistribution and stacking order vary under distinct moiré periodicities, and what role quasiparticle dynamics play in such synergistic superlattices.

Here, we report an engineered heterotrilayer combining an R-stacked top bilayer and an H-stacked bottom bilayer with mismatched moiré wavelengths, resulting in a bichromatic moiré superlattice formed by the interference of two distinct moiré periods. This unique lattice geometry gives rise to emergent phenomena not accessible in conventional moiré systems. First, the hybridized moiré potentials support a new class of charged excitons—fermionic quadrupolar moiré trions—which are distinct from previously reported bosonic quadrupolar excitons. These trions exhibit electrically tunable dipole moments, enabling controlled studies of quasiparticle dynamics in complex potential landscapes. Second, bichromatic interference enables in-situ tunability of the beating periodicity, dynamically reshaping the carrier-trapping landscape. We observe an electric-field-driven transition from an interlayer Mott insulating state to an intralayer Mott state with enhanced on-site Coulomb repulsion. Further tuning modifies the moiré potential profile and shifts the density of ground-state sites, allowing precise control over electron correlations and establishing the asymmetric heterotrilayer as a reconfigurable platform for exploring programmable correlated quantum states. Finally, the coexistence of R- and H-stacked domains enables tailored control of interlayer excitonic selection rules, advancing the engineering of spin-photon coupling for quantum optoelectronic applications.

Results

Structures of R- and H-stacked $WSe_2/WS_2/WSe_2$ heterotrilayers

We fabricated dual-gate $WSe_2/WS_2/WSe_2$ heterotrilayer devices, which allow independent control of doping levels and vertical electric field (Fig. 1a, see Methods). The structure of heterotrilayers investigated is shown in Fig. 1b inset. We highlight the layer alignments with arrows: parallel indicating R stacking and opposite indicating H stacking. Device 1 (Fig. 1b optical image) displays the top WSe_2 layer aligned with the middle WS_2 layer at an angle close to 1° (R stacking), while the bottom WSe_2 layer is rotated 180° with a slightly different alignment angle (H stacking). This device also includes a bilayer region for direct comparison.

Moiré superlattices can be clearly identified in the Piezoresponse Force Microscopy (PFM) image of Device 1's trilayer region (Fig. 1c). Fourier transform data (Fig. 1c inset) reveal two distinct moiré superlattices with lattice constants approximately 7.4 nm (~ 0.9°) and 6.7 nm (~ 1.5°). Besides, a larger superlattice background could be identified in the PFM image emerging from the interference of these two sets. This small, deliberate twist-angle offset of roughly 0.5° keeps each bilayer well aligned and prevents severe global disorder and frustration, while preserving the beating patterns (see Supplementary Information Fig. S1).

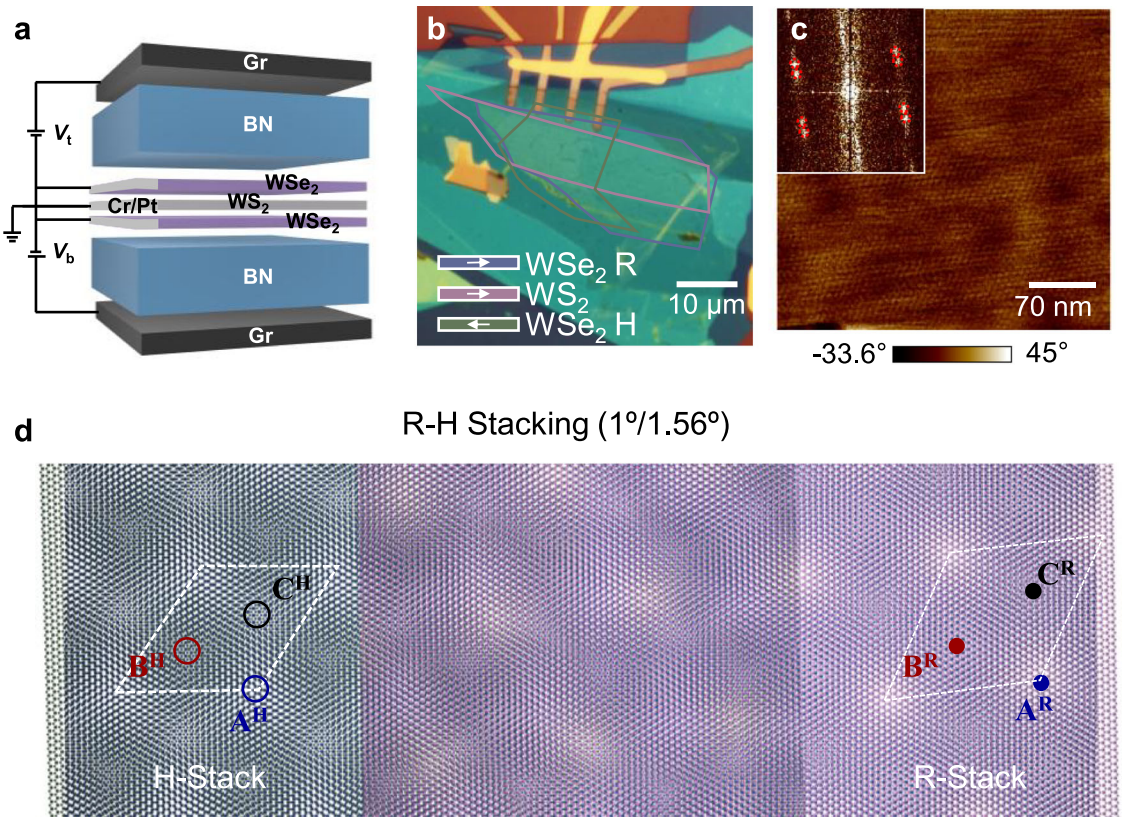

Fig. 1 | Structural characterization of trilayer heterostructure Device 1. **a** Schematic of a dual-gated $WSe_2/WS_2/WSe_2$ heterotrilayer device, in which pre-evaporated and AFM-cleaned Cr/Pt is used as contacts to the TMD layers. **b** Optical image of Device D1 highlights the alignment of top WSe_2 and bottom WSe_2 layers relative to the middle WS_2 layer, with the top WSe_2, middle WS_2, and bottom WSe_2 outlined in purple, pink, and green, respectively. Inset: Schematic illustrating layer alignments with arrows indicating R stacking (parallel) and H stacking (opposite). **c** PFM image of Device D1's trilayer region, revealing two distinct moiré superlattices with lattice constants of approximately 7.4 nm (~ 0.9°) and 6.7 nm (~ 1.5°), marked with red dashed circles in the inset Fourier transform image. **d** An exemplary trilayer with a top moiré with a 1° rotation (R-stack) and a bottom moiré with a 1.56° rotation (H-stack), with high-symmetry sites A, B, C denoted by blue, red, and black circles; hollow symbols mark H-stack sites (A^H, B^H, C^H) and filled symbols mark R-stack sites (A^R, B^R, C^R). The R- and H-stack moiré superlattices form a concatenated moiré pattern across the trilayer.

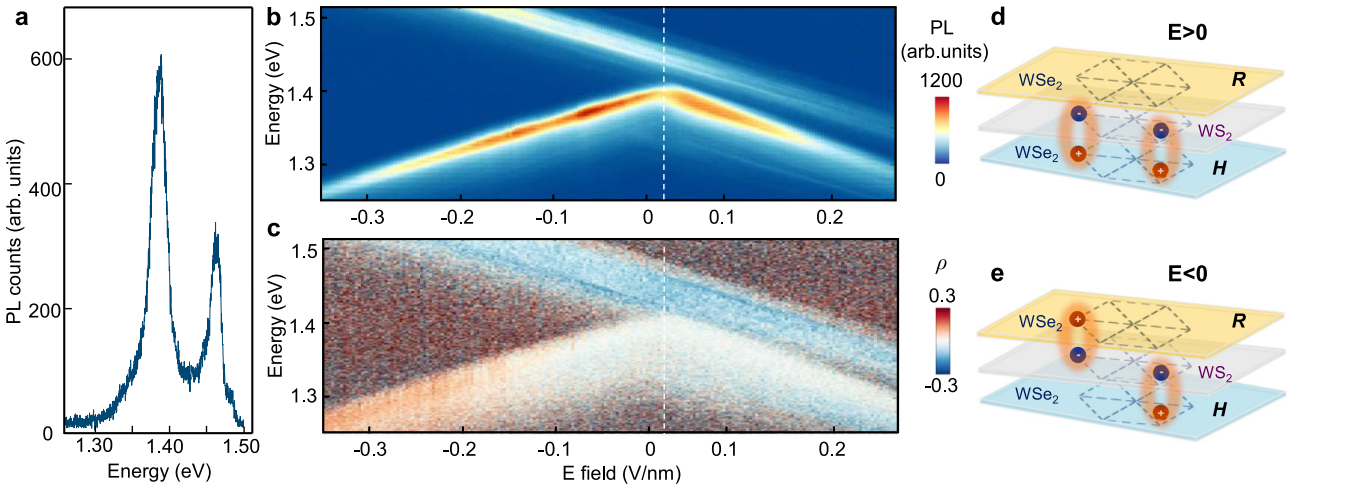

Fig. 2 | Electric field dependence of interlayer PL peaks. a PL spectrum of the trilayer heterostructure, displaying a dominant low-energy peak at 1.39 eV (low-energy peak) and a secondary peak at 1.46 eV (high-energy peak). **b** Interlayer PL as a function of electric field without external doping possesses different slopes of the Stark shift across positive and negative electric field regimes. **c** The corresponding PL degree of circular polarization $\rho = \frac{\sigma^+/\sigma^+ - \sigma^+/\sigma^-}{\sigma^+/\sigma^+ + \sigma^+/\sigma^-}$ in the same conditions as in **b**. The high-energy peak remains cross-polarized regardless of field direction, whereas the low-energy peak flips from cross- to co-polarized when the electric field is reversed from positive to negative. **d**-**e**, Schematics of preferred sites of interlayer exciton emission with positive electric field (**d**) and negative electric field (**e**). The yellow, grey, and blue layers denote top WSe_2 (R stacking), middle WS_2, and bottom WSe_2 (H stacking). Blue and red spheres indicate electrons and holes, respectively. The low-energy peak originates from sites where holes can redistribute freely between the top and bottom WSe_2 layers (the left side in **d**, **e**), whereas the high-energy peak comes from sites where holes remain localized in the bottom WSe_2 layer (the right side in **d**, **e**). In this study, positive electric field points from the top WSe_2 to the bottom WSe_2, and negative electric field points from the bottom WSe_2 to top WSe_2 layer.

Unlike previous experimental studies focusing on symmetric alignment in the top and bottom heterostructures[37–39], the intricate interplay of high-symmetry stacking configurations in the R-H misaligned heterotrilayers unveils the elusive atomic registry textures. As depicted in Fig. 1d, an exemplary trilayer exhibits a top moiré with a 1° rotation (R-stack) and a bottom moiré with a 1.56° rotation (H-stack). Following the convention from Tong et al[36], these R- and H-stack moiré superlattices form a concatenated moiré pattern across the trilayer, delineated by nine distinct high-symmetry locales (Supplementary Information Fig. S2), each exhibiting different band hybridization between the top and bottom layers. At locales such as A^R/A^H (similar for B^R/B^H, C^R/C^H in Fig. S2), conservation of spin-valley degrees of freedom is anticipated to suppress tunneling and hybridization. By contrast, high-symmetry locales such as A^R/C^H may allow stronger hybridization, depending on the local atomic alignment.

In reported heterobilayers, the spatial distributions of band-edge electrons differ between R-stack and H-stack heterostructures[40]. In R-stack heterobilayers, electrons are localized predominantly at the high-symmetry location C^R, whereas in H-stack heterobilayers, they are mostly found at location A^H. Combining R and H stackings in heterotrilayers likely generates multiple orbital configurations for electrons centered in the middle layer, where both A and C serve as trapping sites. The physics inherent in R-H style heterotrilayers promises a tapestry of intriguing phenomena.

Multi-orbital nature of the bichromatic moiré superlattice

The multi-orbital nature of the bichromatic moiré superlattice promotes the tunability of valley and spin degrees of freedom in TMD heterotrilayers. Experimentally, this manifests as multiple photoluminescence (PL) peaks in the heterotrilayer structure. The PL spectrum (Fig. 2a) reveals a dominant low-energy emission at ~1.39 eV and a secondary, weaker peak at ~1.46 eV. The energy separation of ~70 meV between the two peaks significantly exceeds the expected exciton double occupancy energy (~ 30 meV) at a single moiré site[26], indicating a multi-orbital origin. Power-dependent PL measurements on Device 3 (Fig. S3) show that both peaks persist even at the low excitation power, confirming their intrinsic origin from the heterotrilayer moiré potential rather than from power-induced filling effects. The normalized power dependence of the lower energy peak (Fig. S4) shows significant saturation behavior. The above evidence confirms that the emissive excitonic species from heterotrilayer regions are intrinsic to the bichromatic moiré potential.

To probe the origins of the dual PL peaks, we conducted out-of-plane electric field measurements while keeping the doping fixed. Upon applying an electric field without external doping, both PL peaks exhibit clear linear Stark shifts (Fig. 2b). These linear Stark shifts correspond to the emissions originating from the interlayer excitons possessing significant out-of-plane dipoles.

The emission energy of the high-energy peak decreases monotonically with the applied electric field. This peak is attributed to the interlayer exciton, with its dipole moment oriented downward. The interlayer exciton arises from the binding of holes in the bottom WSe_2 layer and electrons in the middle WS_2 layer. Polarization analysis, shown in Fig. 2c, further supports the identification of this high-energy exciton. The peak exhibits cross-polarization ($\rho < 0$), indicating that the emission originates from an H-stack WSe_2-WS_2 heterobilayer[40]. This agrees with mid-bottom bilayer configuration.

In contrast, the low-energy peak shows opposite slopes when the sign of the electric field is reversed. These opposing slopes, observed in Fig. 2b, c, correspond to dipole moments that flip direction. This behavior confirms that the lower-energy exciton exhibits a bipolar emission characteristic. The dipole moment of this interlayer exciton (IX) flips dynamically with the applied electric field, with hole polarization occurring either in the top R-stacked layer or the bottom H-stacked layer (as shown in Fig. 2d, e).

At a small electric field near $E = 0.02$ V/nm, the low-energy interlayer excitons emitted from the top R-stacked and bottom H-stacked layers exhibit identical energies. In this range, the local slope of the low-energy peak is flat. This flat slope matches the quadrupolar excitons observed in symmetric heterotrilayers[37–39]. Despite differences in periodicity and stacking order between the top and bottom moiré superlattices, the identical energies and flat local slope are a signature of a shared ground state in the R-H aligned heterotrilayers. Additional

https://doi.org/10.1038/s41467-025-65342-6

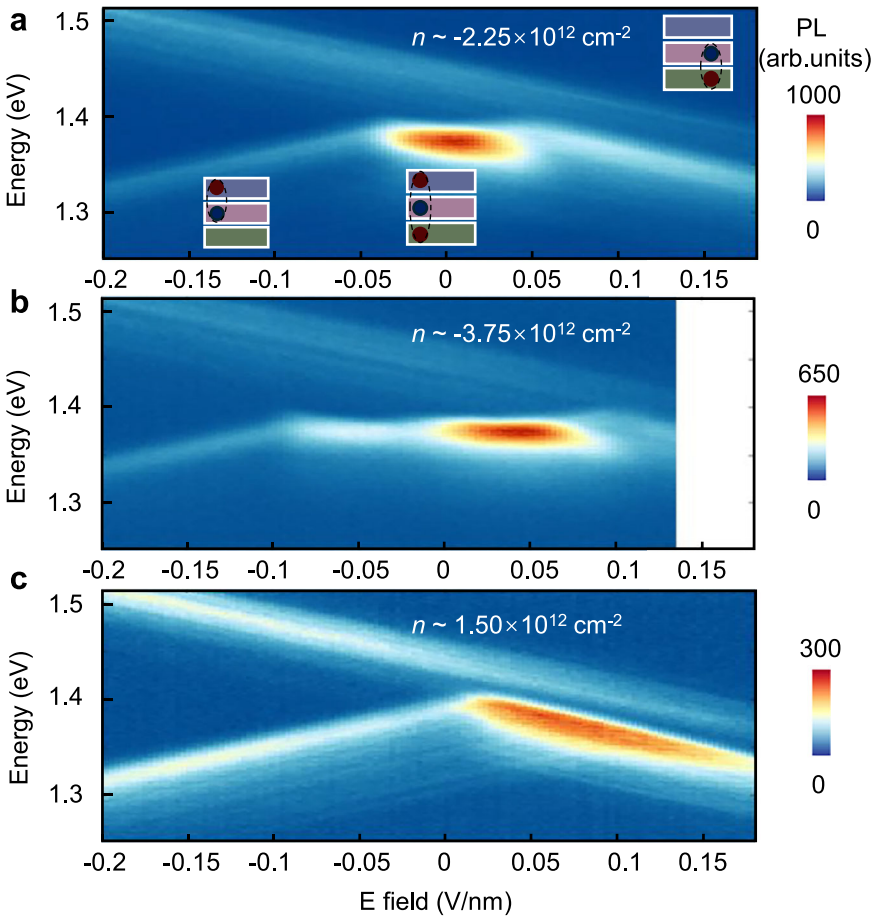

Fig. 3 | PL peaks' positions shift as a function of the electric field under fixed doping conditions. a $n = -2.25 \times 10^{12}\,cm^{-2}$, **b**, $n = -3.75 \times 10^{12}\,cm^{-2}$, **c**, $n = 1.5 \times 10^{12}\,cm^{-2}$. Under hole doping (**a** and **b**), the peak energy of the low-energy peak remains nearly constant over a finite electric-field window, indicating the stabilization of a quadrupolar trion, whereas no such signature appears under electron doping (**c**). The inset of **a** schematically present, from right to left, the carrier configurations that yield the low-energy peak: holes localized in the bottom WSe_2 layer under positive electric field and pair with an electron in the middle WS_2 layer to form an interlayer exciton; holes shared between the top and bottom WSe_2 layers create a quadrupolar trion; and holes once again confined to the top WSe_2 layer bind to the middle-layer electron under negative electric field, forming another interlayer exciton. The blue and red circles represent electrons and holes located in the WS_2 and WSe_2 layers, respectively. The blue, pink and green rectangles denote the top WSe_2, middle WS_2 and bottom WSe_2 layers.

data from another Device D2 is present in Supplementary Information Fig. S5.

The unique features of the PL peaks are attributed to the multi-orbital characteristics of the heterotrilayers. As illustrated in Fig. S2, the heterotrilayers feature multiple high-symmetry sites arising from the beating of the top and bottom moiré superlattices. Excitation of intralayer excitons in WSe_2 leads to rapid carrier relaxation to the band edges, forming interlayer excitons. At minimally hybridized sites, the excitons retain the same dipole moment. As a result, excitons emitted from these sites exhibit a single slope, as shown in Fig. 2b. By contrast, at strongly hybridized sites the lowest-energy state is shared by both the top and bottom layers. In this case, an applied electric field polarizes holes toward the bottom WSe_2 layer (for $E > 0$) or the top WSe_2 layer (for $E < 0$). Consequently, the bound excitons at these sites develop a positive or negative dipole moment depending on the direction of the electric field.

Although the excitons share the same lowest-energy at specific high-symmetry locations, the distinct stacking orders of the top and bottom bilayers enforce opposing selection rules. The low-energy PL peak for $E < 0$, characterized by a positive slope, exhibits a positive degree of polarization (Fig. 2c), which is consistent with the R-stack configuration in the upper heterobilayer of our device. In contrast, interlayer excitons in the lower heterobilayer, with negative slopes, display a negative degree of polarization, aligning with the H-stack configuration. This layer-polarized emission introduces an additional degree of freedom for manipulating circular polarization while maintaining fixed emission energies.

Quadrupolar moiré trions

Under hole-doping conditions, our experiments reveal the presence of quadrupolar excitonic emission in the moiré trilayers, as shown in Fig. 3a, b. Additional data across varying doping conditions from Device D1 are presented in Fig. S6. Furthermore, data from Device D2, tested under similar conditions, is included in Fig. S7. The formation of quadrupolar excitonic species occurs immediately upon introducing excess holes into the heterostructure. To confirm the formation of interlayer trions, we deliberately dope the heterotrilayer at fixed hole concentrations while sweeping the electric field. Figures 3a, b show two hole-doping conditions at $n = -2.25 \times 10^{12}\,cm^2$ and $n = -3.75 \times 10^{12}\,cm^{-2}$. The low-energy peak exhibits minimal shifts in emission energy under low-field conditions (additional hole doping scenarios are shown in Fig. S6). The flat slope confirms an almost negligible out-of-plane dipole moment. In contrast, the high-energy peak shifts negatively with the electric field, consistent with the behavior observed in Fig. 2b under intrinsic doping conditions. This shift is attributed to the fixed out-of-plane dipole moment of the exciton, whose position in the moiré superlattice results in a small hybridization probability, as illustrated in Fig. 2d, e.

https://doi.org/10.1038/s41467-025-65342-6

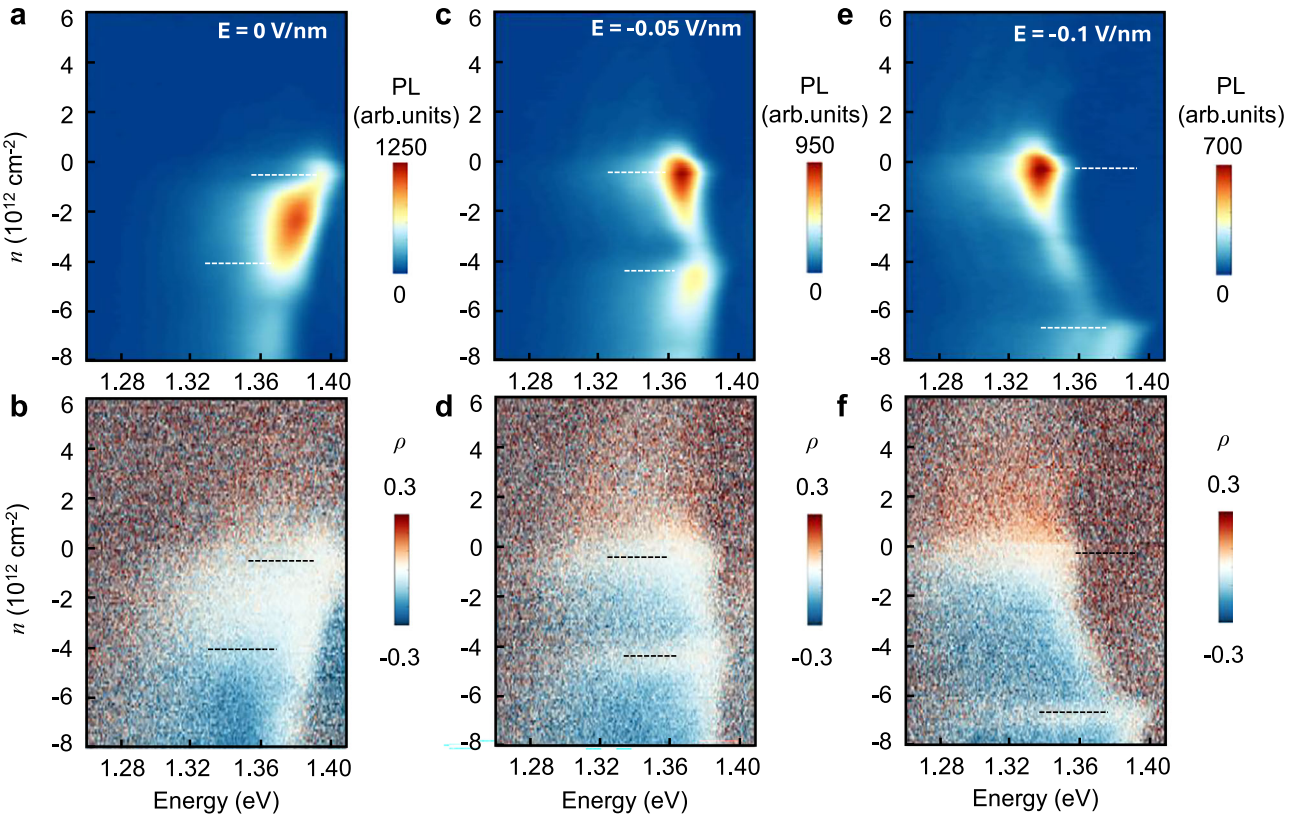

Fig. 4 | PL intensity and polarization as a function of doping with a fixed electric field. a–**b**, PL intensity (**a**) and polarization (**b**) versus density with $E = 0$ V/nm. **c**–**d**, PL intensity (**c**) and polarization (**d**) versus density with $E = -0.05$ V/nm. **e**–**f**, PL intensity (**e**) and polarization (**f**) versus density with $E = -0.1$ V/nm. The PL intensity and polarization changes are used to identify the integral filling and insulating states, $\nu = 0$ and $\nu = -1$ can be clearly discerned and marked by dashed lines in both the PL (white dashed lines) and corresponding polarization (black dashed lines) 2D maps. The corresponding density in $\nu = -1$ under the electric field of 0 V/nm, −0.05 V/nm and −0.1 V/nm is 3.6×10^{12} cm^{-2}, 4×10^{12} cm^{-2} and 6.45×10^{12} cm^{-2}, respectively. Line cuts of the raw data illustrating the polarization changes under specific conditions are provided in the Supplementary Information as Fig. S11.

Under electron doping conditions, the flat slope of the low-energy peak is absent (Fig. 3c). The observed slopes are directly ascribed to the dipoles associated with the top and bottom interlayer excitons.

We attribute the excitonic species with nearly zero out-of-plane dipole moments to the formation of quadrupolar moiré trions under hole-doped conditions. This interpretation is consistent with a scenario in which two holes are symmetrically distributed across the WSe_2 layers (Fig. 3a middle inset), regardless of whether the structure is R-stack or H-stack aligned. Strong Coulomb interactions drive the emergence of this unique three-particle complex, where two holes and one electron are strongly localized at the shared high-symmetry moiré sites. The resulting interlayer quadrupolar trion exhibits a nearly vanishing out-of-plane dipole moment, and its energy remains stable under varying electric fields, clearly distinguishing it from previously reported interlayer trions in heterobilayers[8,9,41]. Importantly, unlike the bosonic quadrupolar excitons observed in symmetric trilayers[37–39] that exist primarily under charge-neutral conditions, quadrupolar moiré trions appear only under doping. Furthermore, they require a substantially larger electric field to polarize into dipole configurations. This enhanced robustness indicates that the formation of interlayer quadrupolar moiré trions is energetically favored in bichromatic heterotrilayers.

When the electric field becomes sufficiently strong, holes in the bottom (top) WSe_2 layer are polarized to the top (bottom) WSe_2 layer to minimize the total energy, resulting in a well-defined out-of-plane dipole moment. Specifically, for hole density below -2×10^{12} cm^{-2} ($\sim \nu = -1$ for one moiré), a modest electric field of approximately ±0.025 V/nm is sufficient to transform the quadrupolar trion into a dipolar exciton (Fig. S6d, e). In this regime, polarized holes can redistribute across different moiré sites within the same WSe_2 layer, effectively lowering the total energy. However, at higher hole fillings $\nu \geq -1$, polarizing all holes into the same layer forces them to share moiré sites, incurring strong on-site Coulomb repulsion. Consequently, a larger field exceeding ±0.05 V/nm is needed to overcome this repulsion and achieve full dipolar polarization. These experimental findings demonstrate that the electric field can effectively tune the ground states of holes by manipulating their layer-specific degrees of freedom.

Electric-field modulation of the moiré potential landscape

We now deliberately tune the electric field to control the distribution of doped holes. As shown in Fig. 4a, b, at $E = 0$ V/nm, the shared ground state results in an even hole distribution across the top and bottom layers, with both WSe_2 layers experiencing the same moiré potential landscape. When the carrier density reaches 3.6×10^{12} cm^{-2}, we observe a change in PL intensity (Fig. 4a) and enhanced polarization (Fig. 4b). This behavior aligns with the formation of an interlayer Mott insulating state, as reported by Lian et al[39]. However, in our study, this phenomenon occurs in an asymmetric heterotrilayer, characterized by distinct R-stack and H-stack layers, contrasting with the symmetric R-R stack with identical lattice constants in the top and bottom layers as described in previous work[39]. It's worth noting that, the interlayer Mott insulating state observed here differs from the behavior seen in regions with only bilayer R-stack heterostructure. In the R-stack heterobilayer, as shown in Fig. S8, holes are strictly confined to the top WSe_2 layer, and intensity variations occur at both fractional and integer filling factors.

https://doi.org/10.1038/s41467-025-65342-6

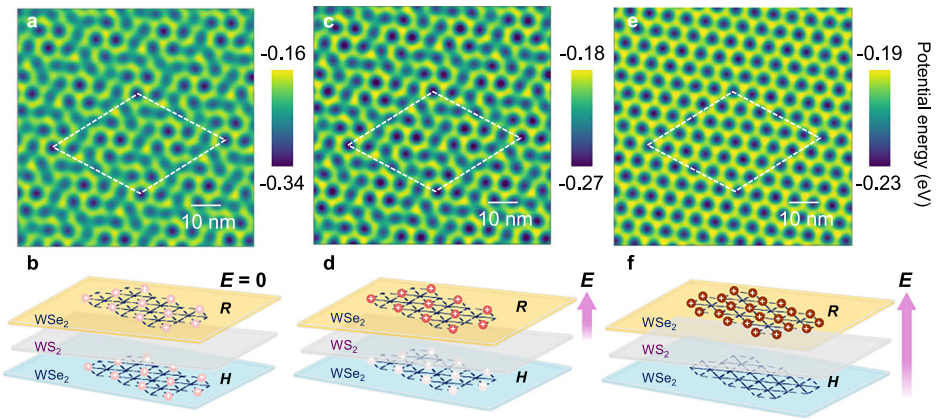

Fig. 5 | Calculated electric-field modulation of moiré superlattice potential landscape in real space. Moiré superlattice potential in the heterotrilayer without electric field (**a**), at electric field of −0.05 V/nm (**c**), and at electric field of −0.1 V/nm (**e**). The bright yellow locales are potential minima for holes. **b**,**d**,**f**, Schematics showing the preferred layer localization of holes under the corresponding electric field conditions. As the out-of-plane electric field is swept from 0 to −0.05 V/nm and then to −0.1 V/nm, the number of hole-potential minima increase significantly, and the hole distribution shifts toward the top WSe_2 layer, accompanied by a transition of the Mott insulating state from interlayer to intralayer. The yellow, grey, and blue slabs represent the top WSe_2 (R stack), middle WS_2, and bottom WSe_2 (H stack) layers, respectively. Colored spheres indicate holes localized in two WSe_2 layers, with darker shading corresponding to higher hole density.

When a fixed negative electric field (−0.05 V/nm) is applied, the doped holes would predominantly occupy the top WSe_2 layer. At a hole carrier density of $4 \times 10^{12}\,cm^{-2}$, strong intensity modulation (Fig. 4c), and a significant decrease in polarization (Fig. 4d) are observed, as labelled by the dashed lines. The observed intensity and polarization modulations are consistent with previously reported signatures of correlated states in TMD heterobilayers[19,25–27,40,42]. It is worth noting that the emergence of integer-filling correlated states provides compelling evidence that the PL peaks originate from excitons localized at bichromatic moiré sites. The abrupt changes in PL intensity and polarization with doping, as shown in Fig. 4 and Figs. S8-10, are indicative of strong interactions between interlayer moiré excitons and correlated electronic states, consistent with prior observations in moiré systems[19,25–27,40,42].

By further tuning the electric field, the moiré potential profile is significantly altered, as shown in Fig. 4e, f. For a fixed electric field of −0.1 V/nm, we observe a surprising increase in the doping density required to reach the insulating state, rising to approximately $6.45 \times 10^{12}\,cm^{-2}$. Furthermore, a distinct blueshift is observed at this point, indicative of the onset of on-site Coulomb repulsion. The substantial increase in carrier density needed to form the insulating state strongly suggests a shift in the density of ground-state sites.

Similar behavior is observed in Device D2 (Fig. S9). The electric field required to reshape the entire moiré landscape is slightly different, owing to the variation in twist angles between the R-stack and H-stack layers. As shown in Fig. S10, the moiré superlattice of the H-stack heterobilayer is approximately 7.6 nm, which is slightly larger than the value measured in Device D1 from the PFM data. However, qualitatively, the behavior with the applied electric field remains consistent with what we observed in Device D1.

To gain insight into the experimental observations, we have calculated the moiré potentials for valence band holes in heterotrilayer bichromatic superlattices, following the methodology outlined by Tong et al[36]. Detailed calculations are provided in the Supplementary Information. The concatenated moiré pattern is visualized by tracing several high-symmetry stacking sites, as shown in Supplementary Fig. S1, which includes both R-stack and H-stack high-symmetry regions. The calculated moiré potentials under various electric field conditions are presented in Fig. 5. The bright regions represent the local potential minima for holes (i.e., the valence band maximum). These regions will be first populated when the system is hole-doped.

Considering the geometry of the trilayer moiré superlattice (Fig. 1d), we find that the heterotrilayer exhibits distinct moiré potential profiles compared to heterobilayers, with the added advantage of dynamic tunability via an applied electric field (Fig. 5). The simulations in Fig. 5 are performed under similar conditions to the measurements in Fig. 4. In Fig. 4a, b, the applied electric field is zero. At this condition, the hole density corresponding to the first integer filling insulating state, identified as an interlayer Mott insulator, is approximately $3.6 \times 10^{12}\,cm^{-2}$, which is notably higher than the density required to reach $\nu = 1$ in the R-type heterobilayer with a moiré wavelength of 7.4 nm ($n \sim 2.1 \times 10^{12}\,cm^{-2}$). In the absence of an electric field, the simulated moiré potential (Fig. 5a) shows bright regions slightly larger than the R-type stacking domains (Fig. S12), with multiple high-symmetry sites available for hole occupancy. As shown in Fig. 5b, the holes are distributed across both the upper and lower WSe_2 layers, forming a degenerate interlayer configuration. Laterally, the hole is confined to a common moiré potential minimum shared between layers, resulting in one hole occupying a shared ground state at the same high-symmetry moiré site in the hybridized trilayer. This correlated state is referred to as an interlayer Mott insulator[39]. In this regime, the holes can redistribute between the top and bottom WSe_2 layers within the same vertical moiré cells.

As the electric field increases (*E*-field pointing from the bottom gate to the top gate) to −0.05 V/nm, the hole density required for the Mott insulating state increases to $4.0 \times 10^{12}\,cm^{-2}$ (Fig. 4c, d). The corresponding simulation shows the area of the bright regions expands slightly, indicating an enhanced capacity for hole occupancy (Fig. 5c). In this regime, holes preferentially occupy sites in the upper layer, with fewer holes residing in the lower layer (Fig. 5d). At an even higher electric field of −0.1 V/nm, the hole density at $\nu = -1$ further increase to $6.45 \times 10^{12}\,cm^{-2}$ (Fig. 4e, f). The simulated potential landscape evolves into a honeycomb-like pattern (Fig. 5e), effectively doubling the number of sites available for hole localization, consistent with our experimental observations. In this regime, the electric field fully polarizes the doped holes to localize in the upper layer (Fig. 5f), where the correlated states are now governed by intralayer hole interactions with modified moiré periodicity and enhanced Coulomb repulsion. The strong on-site repulsion energy results in a significant blueshift in the excitonic emission. Overall, these results demonstrate that the applied electric field in a bichromatic moiré superlattice enables a tunable transition from interlayer- to intralayer-dominated Mott insulating states.

We realize that the role of strain relaxation in real devices would affect the moiré superlattice landscape. In complex trilayer structures, the R-stack and H-stack regions relax strain differently[40]. However, our calculations provide a qualitative physical framework for understanding the role of the electric field in modulating moiré potentials and hole distribution within the superlattices. These findings strongly support the realization of electrically tunable bichromatic moiré potentials.

Discussion

In conclusion, we have demonstrated tunable excitonic and electronic states in uniquely engineered asymmetric R-H $WSe_2/WS_2/WSe_2$ bichromatic superlattices with two interfering moiré wavelengths. This configuration provides access to previously unexplored physical phenomena. First, the bichromatic superlattice hosts fermionic quadrupolar moiré trions, distinct from the bosonic quadrupolar excitons reported earlier. Second, both excitonic states and electronic ground states in these lattices can be highly tuned by external electric fields. Third, optical selection rules can be conveniently tailored within a single device. By carefully engineering stacking configurations in heterostructures, we demonstrate that quantum states in bichromatic moiré superlattices can be controlled and reconfigured, opening new pathways for investigating many-body physics in quantum materials.

Our findings open exciting possibilities for further investigation into the dynamics of multi-orbital excitons and other quasiparticles in more complex moiré superlattices. Future experiments would aim to explore the coevolution of multiple moiré potentials, particularly in trilayer systems with different stacking orders/angles, and their impact on charge/exciton interactions and quantum phases. The ability to independently control multiple moiré superlattices holds the potential for realizing dynamically tunable quantum systems, with applications in quantum simulation, topological phases, and novel optoelectronic devices.

The emission of these quadrupolar excitons and trions involves a superposition of two excitonic species with dipole moments oriented in opposite directions. The investigation of the coherence and entanglement could provide new avenues for the manipulation of quantum light. Quadrupolar trions reported in this work are particularly robust against electrical noise under highly hole-doped conditions, which could emerge as promising stable sources.

Methods

Sample fabrication

The sample fabrication details can be found in Ref.[43] In brief, a prefabricated bottom gate (a hexagonal boron nitride (hBN)/graphite stack) was transferred, and platinum contacts were defined above the stack using electron beam lithography. Subsequently, 3/7 nm of Cr/Pt was deposited via electron beam evaporation to form the bottom contacts. The bottom gate with contacts was then cleaned using an atomic force microscope (AFM) operated in contact mode.

Monolayer WS_2 and WSe_2 flakes were mechanically exfoliated from bulk crystals. The WSe_2 crystals were grown using the flux method, while the WS_2 crystals were sourced from HQ Graphene. Prior to stacking, the crystal orientations of the monolayers were determined via linear polarization-resolved second harmonic generation to ensure accurate alignment. To achieve the desired R- and H-stacking configurations, the top and bottom WSe_2 monolayers were taken from the same large flake, which was precisely cut using an AFM probe to minimize strain introduced by conventional tear-and-stack methods.

The monolayers were then assembled using a flat polycarbonate (PC)/polydimethylsiloxane (PDMS) stamp and transferred onto the cleaned bottom gate. Twist angles were confirmed using Piezo-response Force Microscopy (PFM)[43,44]. PFM was carried out using a Bruker Dimension Icon AFM and Asylum Research Cypher S AFM with Pt–Ir-coated conductive probes (SCM-PIT-V2, force constant ≈ 3 N/m). An a.c. bias (< 300 mV, ≈700 kHz and 350 kHz for lateral and vertical resonance frequencies, respectively) was applied between tip and sample, and the induced deformation amplitude and phase were recorded to probe the local electromechanical response. Once the moiré wavelength was determined, a top graphite/hBN stack was transferred for encapsulation and to complete the dual-gate geometry. Finally, Cr/Au electrodes for wire bonding were patterned using electron beam lithography and deposited via e-beam evaporation (7/70 nm Cr/Au).

Optical measurements

PL measurements were performed using a home-built confocal microscope in reflection geometry. The sample was mounted in a close-cycled cryostat with temperature kept at 5 K (Montana CryoAdvance 50), unless otherwise specified. A helium-neon laser (1.96 eV) was used in PL measurements. An additional 650 nm short pass filter has been used to filter out any side bands. The excitation power for PL measurement was kept at 1 μW. The incident polarization was set to be σ^+ polarized using a linear polarizer and quarter-wave plate, while the photoluminescence was collected and polarization-resolved to σ^+ or σ^- using another quarter-wave plate on a rotational mount and a linear polarizer. PL signals were dispersed by a diffraction grating and detected on a silicon charge-coupled device camera. The PL was spectrally filtered from the laser using a 700-nm long-pass filter before being directed into a spectrometer. A pinhole was used in the collection path to exclude signals from outside the laser spot area.

Calculation of carrier density and electric field

The carrier density is estimated using a parallel-plate capacitor model with the gate voltage applied. The BN thickness of samples was measured by AFM. D1 has 16 nm for top BN flake and 20 nm for the bottom BN flake. And the top and bottom BN thickness of D2 are ~27.5 nm. The carrier density is calculated using $C_t\,\Delta V_t + C_b\,\Delta V_b$, where C_t (C_b) is the geometric capacitance of top (bottom) gate, and ΔV_t (ΔV_b) is the effective doping voltage (the relative voltage from band edge). The value used for the dielectric constant of BN is $\varepsilon_{hBN} \approx 3$. The moiré wavelength λ was derived directly from PFM images, and the corresponding moiré density is given as $n_0 \approx 2 / (\sqrt{3}\,\lambda^2)$. The filling factor was calculated as $\nu = n/n_0$ and compared with the assignment of integer filling factors based on gate-dependent photoluminescence in well-understood heterobilayer region in the same sample.

The perpendicular electrical displacement field D is calculated using $D = (C_t\,\Delta V_t - C_b\,\Delta V_b)/2$ and the electric field is calculated as $E = D/\varepsilon_0$.

Theoretical calculations

The moiré potential energies are described in terms of the lowest several harmonics[36,45], wherein the parameters are determined by the high-symmetry stackings (See Supplementary Information for more details). All data for the high-symmetry stackings is extracted from first-principles calculations that are performed using the Vienna ab initio Simulation Package (VASP)[46].

Data availability

The Source Data underlying the figures of this study are available with the paper. All other datasets generated and/or analyzed during this study are available from the corresponding author upon request. Source data are provided as Source Data files. Source data are provided with this paper.

References

1. Xue, J. et al. Scanning tunnelling microscopy and spectroscopy of ultra-flat graphene on hexagonal boron nitride. *Nat. Mater.* **10**, 282–285 (2011).

2. Decker, R. et al. Local Electronic Properties of Graphene on a BN Substrate via Scanning Tunneling Microscopy. *Nano Lett.* **11**, 2291–2295 (2011).
3. Yankowitz, M. et al. Emergence of superlattice Dirac points in graphene on hexagonal boron nitride. *Nat. Phys.* **8**, 382–386 (2012).
4. Jin, C. et al. Observation of moiré excitons in WSe2/WS2 heterostructure superlattices. *Nature* **567**, 76–80 (2019).
5. Seyler, K. L. et al. Signatures of moiré-trapped valley excitons in MoSe2/WSe2 heterobilayers. *Nature* **567**, 66–70 (2019).
6. Tran, K. et al. Evidence for moiré excitons in van der Waals heterostructures. *Nature* **567**, 71–75 (2019).
7. Ruiz-Tijerina, D. A. & Fal'ko, V. I. Interlayer hybridization and moiré superlattice minibands for electrons and excitons in heterobilayers of transition-metal dichalcogenides. *Phys. Rev. B* **99**, 125424 (2019).
8. Liu, E. et al. Signatures of moiré trions in WSe2/MoSe2 heterobilayers. *Nature* **594**, 46–50 (2021).
9. Wang, X. et al. Moiré trions in MoSe2/WSe2 heterobilayers. *Nat. Nanotechnol.* **16**, 1208–1213 (2021).
10. Li, W., Lu, X., Dubey, S., Devenica, L. & Srivastava, A. Dipolar interactions between localized interlayer excitons in van der Waals heterostructures. *Nat. Mater.* **19**, 624–629 (2020).
11. Wu, F., Lovorn, T., Tutuc, E. & MacDonald, A. H. Hubbard Model Physics in Transition Metal Dichalcogenide Moiré Bands. *Phys. Rev. Lett.* **121**, 026402 (2018).
12. Tang, Y. et al. Simulation of Hubbard model physics in WSe2/WS2 moiré superlattices. *Nature* **579**, 353–358 (2020).
13. Xu, Y. et al. A tunable bilayer Hubbard model in twisted WSe2. *Nat. Nanotechnol.* **17**, 934–939 (2022).
14. Götting, N., Lohof, F. & Gies, C. Moiré-Bose-Hubbard model for interlayer excitons in twisted transition metal dichalcogenide heterostructures. *Phys. Rev. B* **105**, 165419 (2022).
15. Gao, B. et al. Excitonic Mott insulator in a Bose-Fermi-Hubbard system of moiré WS2/WSe2 heterobilayer. *Nat. Commun.* **15**, 2305 (2024).
16. Zhou, Y. et al. Bilayer Wigner crystals in a transition metal dichalcogenide heterostructure. *Nature* **595**, 48–52 (2021).
17. Xu, Y. et al. Correlated insulating states at fractional fillings of moiré superlattices. *Nature* **587**, 214–218 (2020).
18. Regan, E. C. et al. Mott and generalized Wigner crystal states in WSe2/WS2 moiré superlattices. *Nature* **579**, 359–363 (2020).
19. Miao, S. et al. Strong interaction between interlayer excitons and correlated electrons in WSe2/WS2 moiré superlattice. *Nat. Commun.* **12**, 3608 (2021).
20. Zhang, Z. et al. Correlated interlayer exciton insulator in heterostructures of monolayer WSe2 and moiré WS2/WSe2. *Nat. Phys.* **18**, 1214–1220 (2022).
21. Huang, X. et al. Correlated insulating states at fractional fillings of the WS2/WSe2 moiré lattice. *Nat Phys* 1–5 https://doi.org/10.1038/s41567-021-01171-w (2021).
22. Li, H. et al. Imaging two-dimensional generalized Wigner crystals. *Nature* **597**, 650–654 (2021).
23. Wang, L. et al. Correlated electronic phases in twisted bilayer transition metal dichalcogenides. *Nat. Mater.* **19**, 861–866 (2020).
24. Tang, Y. et al. Dielectric catastrophe at the Wigner-Mott transition in a moiré superlattice. *Nat. Commun.* **13**, 4271 (2022).
25. Lian, Z. et al. Valley-polarized excitonic Mott insulator in WS2/WSe2 moiré superlattice. *Nat. Phys.* **20**, 34–39 (2024).
26. Park, H. et al. Dipole ladders with large Hubbard interaction in a moiré exciton lattice. *Nat. Phys.* **19**, 1286–1292 (2023).
27. Xiong, R. et al. Correlated insulator of excitons in WSe2/WS2 moiré superlattices. *Science* **380**, 860–864 (2023).
28. Ma, L. et al. Strongly correlated excitonic insulator in atomic double layers. *Nature* **598**, 585–589 (2021).
29. Nguyen, P. X. et al. Perfect Coulomb drag in a dipolar excitonic insulator. *arXiv* https://doi.org/10.48550/arxiv.2309.14940 (2023).
30. Zhang, Y., Yuan, N. F. Q. & Fu, L. Moir\'e quantum chemistry: charge transfer in transition metal dichalcogenide superlattices. *Arxiv* https://doi.org/10.1103/physrevb.102.201115 (2019).
31. Park, H. et al. Observation of Fractionally Quantized Anomalous Hall Effect. *Nature* 1–3 https://doi.org/10.1038/s41586-023-06536-0 (2023).
32. Cai, J. et al. Signatures of fractional quantum anomalous Hall states in twisted MoTe2. *Nature* **622**, 63–68 (2023).
33. Xu, F. et al. Observation of Integer and Fractional Quantum Anomalous Hall Effects in Twisted Bilayer MoTe2. *Phys. Rev. X* **13**, 031037 (2023).
34. Zeng, Y. et al. Thermodynamic evidence of fractional Chern insulator in moiré MoTe2. *Nature* **622**, 69–73 (2023).
35. Li, T. et al. Quantum anomalous Hall effect from intertwined moiré bands. *Nature* **600**, 641–646 (2021).
36. Tong, Q., Chen, M., Xiao, F., Yu, H. & Yao, W. Interferences of electrostatic moir potentials and bichromatic superlattices of electrons and excitons in transition metal dichalcogenides. *2d Mater.* **8**, 025007 (2021).
37. Yu, L. et al. Observation of quadrupolar and dipolar excitons in a semiconductor heterotrilayer. *Nat. Mater.* **22**, 1485–1491 (2023).
38. Li, W. et al. Quadrupolar–dipolar excitonic transition in a tunnel-coupled van der Waals heterotrilayer. *Nat. Mater.* **22**, 1478–1484 (2023).
39. Lian, Z. et al. Quadrupolar excitons and hybridized interlayer Mott insulator in a trilayer moiré superlattice. *Nat. Commun.* **14**, 4604 (2023).
40. Wang, X. et al. Intercell moiré exciton complexes in electron lattices. *Nat. Mater.* **22**, 599–604 (2023).
41. Brotons-Gisbert, M. et al. Moiré-Trapped Interlayer Trions in a Charge-Tunable WSe2/MoSe2 Heterobilayer. *Phys. Rev. X* **11**, 031033 (2021).
42. Liu, E. et al. Excitonic and Valley-Polarization Signatures of Fractional Correlated Electronic Phases in a WSe2/WS2 Moiré Superlattice. *Phys. Rev. Lett.* **127**, 037402 (2021).
43. Wang, X. et al. Light-induced ferromagnetism in moiré superlattices. *Nature* **604**, 468–473 (2022).
44. Stansbury, C. H. et al. Visualizing electron localization of WS2/WSe2 moiré superlattices in momentum space. *Sci. Adv.* **7**, eabf4387 (2021).
45. Kresse, G. & Furthmüller, J. Efficient iterative schemes for ab initio total-energy calculations using a plane-wave basis set. *Phys. Rev. B* **54**, 11169–11186 (1996).
46. Kresse, G. & Furthmüller, J. Efficiency of ab-initio total energy calculations for metals and semiconductors using a plane-wave basis set. *Comput. Mater. Sci.* **6**, 15–50 (1996).

Acknowledgements

This work was mainly supported by the Wang Start-up funding, funded by the College of Arts & Sciences at Washington University in St. Louis (WUSTL). The fabrication is partially supported by Ralph E. Powe Junior Faculty Enhancement Awards, partially supported by the Gordon and Betty Moore Foundation, grant https://doi.org/10.37807/gbmf11560. X.W. acknowledges equipment support by the Center for Quantum Leaps at WUSTL. X.W. acknowledges the use of the Cypher S atomic force microscope for high-resolution PFM characterization of the moiré superlattices. The fabrication used instruments in the Institute of Materials Science and Engineering (IMSE) at WUSTL, with partial financial support from IMSE. Bulk WSe_2 crystals were grown and characterized by C.H., J.C., and J.Y. Materials synthesis by C.H. and J.C. was supported as part of Programmable Quantum Materials, an Energy Frontier Research Center funded by the U.S. DOE, Office of Science, BES, under award DE-SC0019443. J.Y. is supported by the US Department of Energy, Office of Science, Basic Energy Sciences, Materials Sciences and Engineering Division. K.W. and T.T. acknowledge support from the Elemental

Strategy Initiative conducted by the MEXT, Japan (Grant Number JPMXP0112101001) and JSPS KAKENHI (Grant Numbers 19H05790, 20H00354 and 21H05233). C.Z. is supported by the Air Force Office of Scientific Research under Grant No. FA9550-20-1-0220 and the National Science Foundation under Grant No. PHY-2409943, OSI-2228725, ECCS-2411394. H.W. and L.Y. are supported by the National Science Foundation (NSF) grant No. DMR-2124934. The simulation used Anvil at Purdue University through allocation DMR100005 from the Advanced Cyberinfrastructure Coordination Ecosystem: Services & Support (ACCESS) program, which is supported by National Science Foundation grants #2138259, #2138286, #2138307, #2137603, and #2138296. E. H. acknowledges support by the Gordon and Betty Moore Foundation, grant https://doi.org/10.37807/gbmf11560.

Author contributions

X.W. conceived the project. X.W., M.C., R.L. fabricated the samples. X.W., M.C., R.L., Y.Y., Y.L. performed the measurements. X.W. analyzed and interpreted the results. H.W., L.Y. and C.Z. performed the calculations. T.T. and K.W. synthesized the hBN crystals. C.H., J.C., and J.Y. synthesized and characterized the bulk WSe_2 crystals. X.W., M.C., H.W., L.Y., C.Z., and E.H. wrote the paper with input from all authors. All authors discussed the results.

Competing interests

The authors declare no competing interests.

Additional information

Supplementary information The online version contains supplementary material available at https://doi.org/10.1038/s41467-025-65342-6.

Correspondence and requests for materials should be addressed to Xi Wang.

Peer review information *Nature Communications* thanks the anonymous reviewers for their contribution to the peer review of this work. A peer review file is available.